Research Article

Crystal Journal of Materials Science & Engineering

CFD Analysis of NACA Airfoils for Wind Turbine and Aerospace Applications at Low Reynolds Numbers

Md. Hasib Mahmud Mazumder[1]*, & Md. Omar Faruq Roney[2]

[1]Department of Mechanical Engineering, Bangladesh University of Engineering and Technology (BUET), Dhaka - 1000, Bangladesh.
[2]Department of Mechanical Engineering, International University of Business Agriculture and Technology (IUBAT), Dhaka - 1230, Bangladesh.

Corresponding Author: Md. Hasib Mahmud Mazumder, Department of Mechanical Engineering, Bangladesh University of Engineering and Technology (BUET), Dhaka - 1000, Bangladesh.

Cite: M. H. M. Mazumder and M. O. F. Roney, "CFD analysis of NACA airfoils for wind turbine and aerospace applications at low Reynolds numbers," Crystal Journal of Materials Science & Engineering, vol. 2, no. 1, pp. 1–11, 2026.

Received: February 14, 2026; **Accepted:** March 09, 2026; **Published:** March 23, 2026

Abstract

This study presents a transition-model-based comparative computational investigation of four symmetric NACA airfoils (0012, 0015, 0018, and 0020) operating at low Reynolds numbers ranging from 3×10^5 to 1×10^6. In this flow regime, transitional effects such as laminar separation and delayed boundary-layer transition significantly influence aerodynamic performance. A two-dimensional steady Reynolds-Averaged Navier–Stokes (RANS) framework was employed using the SST k–ω turbulence model coupled with the γ–Re_θ transition model to improve the prediction of lift and drag characteristics under low-Reynolds-number conditions. A structured C-type mesh with near-wall refinement was generated to ensure accurate boundary-layer resolution. Numerical results were validated against available experimental data, demonstrating good agreement in aerodynamic performance trends within the pre-stall region. The results indicate that aerodynamic efficiency increases with Reynolds number for all profiles due to delayed flow separation and enhanced boundary-layer stability. Among the airfoils investigated, NACA 0012 consistently exhibited the highest lift-to-drag ratios at moderate angles of attack (6°–9°), whereas thicker profiles such as NACA 0018 and 0020 showed comparatively lower aerodynamic efficiency. This work provides a transition-aware comparative assessment of multiple symmetric NACA airfoils across a practical low-Reynolds-number range relevant to small-scale wind turbines and unmanned aerial vehicle (UAV) applications. The findings highlight the importance of airfoil selection where transitional flow effects play a critical role in aerodynamic performance.

Keywords

NACA Airfoils, Reynolds Number, Aerodynamic Performance, Turbulence Model

Introduction

Understanding the aerodynamic performance of wind turbine blades is essential for improving the efficiency of wind energy systems, particularly under low Reynolds number conditions where transitional flow phenomena significantly influence boundary-layer behavior. In this regime, laminar separation, delayed transition, and early stall can substantially alter lift and drag characteristics. Since airfoil geometry directly governs these aerodynamic responses, accurate aerodynamic assessment is critical for optimizing blade design in renewable energy and small-scale aerospace applications.

Horizontal Axis Wind Turbines (HAWTs), with blades rotating parallel to the wind direction, are widely used for large-scale energy generation. In contrast, Vertical Axis Wind Turbines (VAWTs), whose blades rotate orthogonally to the wind flow, are better suited for small-scale or urban environments due to their compact configuration and omnidirectional wind acceptance [1]. In both systems, symmetric NACA 4-digit airfoils are frequently adopted because of their geometric simplicity and balanced aerodynamic characteristics. Among them, the NACA 0012 airfoil has been extensively utilized owing to its favorable lift-to-drag performance across a range of angles of attack. Previous

studies have demonstrated that aerodynamic performance at low Reynolds numbers can be improved through surface modifications such as dimples and dynamic roughness elements, which enhance boundary-layer attachment and delay flow separation [2, 3]. Moderately thick airfoils such as NACA 0015 and NACA 0018 have also been investigated for their structural advantages while maintaining acceptable aerodynamic efficiency [4, 5]. Additionally, the application of flow-control devices, including Gurney flaps and vortex generators, along with comparative turbulence model analyses, has further improved understanding of flow behavior over symmetric airfoils [6–8].

The NACA 0018 airfoil, in particular, has received significant attention due to its sensitivity to stall and laminar separation bubbles at low Reynolds numbers [9, 10]. These investigations consistently highlight the influence of Reynolds number and angle of attack on aerodynamic coefficients, emphasizing the importance of appropriate turbulence modeling for reliable CFD predictions [11]. Although thicker profiles, such as NACA 0020, are less frequently studied, their structural robustness makes them relevant for load-intensive configurations. However, predicting transitional effects at low Reynolds numbers remains challenging. Conventional Reynolds-Averaged Navier–Stokes (RANS) models often struggle to resolve laminar separation bubbles and transition onset, resulting in deviations from experimental observations [12–14]. Studies by Lee et al. [15] and Sato et al. [16] underscore the need for accurate separation modeling, while foundational work by Lissaman [17] and Abbott and von Doenhoff [18] established early understanding of airfoil aerodynamics and transition phenomena.

To improve predictive capability in wind turbine simulations, advanced turbulence modeling approaches have been increasingly adopted. Although URANS-based solvers are frequently used in VAWT analyses, accurately capturing unsteady separation and reattachment remains challenging [19, 23]. The Shear Stress Transport (SST) k–ω model, which blends the near-wall sensitivity of the k–ω formulation with the freestream stability of the k–ε model, has demonstrated improved accuracy in flows with adverse pressure gradients and separation [20, 22]. Comparative CFD investigations have shown that the k–ε Realizable and k–ω SST models perform effectively in two-dimensional aerodynamic simulations [24]. Similarly, Gosselin [27] evaluated Spalart–Allmaras, low-Re k–ω SST, and Transition SST models, identifying k–ω SST as a reliable option across various operating conditions within low Reynolds number ranges [22]. Nevertheless, conventional k–ω and Spalart–Allmaras models may remain limited in resolving laminar separation bubbles [25], even though the SST formulation has demonstrated improved robustness under low-Reynolds-number conditions without requiring additional damping functions [26, 28]. Furthermore, Mazumder [29] emphasized the critical influence of turbulence model selection on aerodynamic prediction accuracy, highlighting the strong performance of SST k–ω and Spalart–Allmaras models in complex flow environments.

Despite extensive investigations of symmetric NACA airfoils, a notable gap persists in systematically incorporating transition-sensitive modeling within the practical Reynolds number range of 3×10^5 to 1×10^6 relevant to small-scale wind turbines and UAV applications. While numerous studies rely on fully turbulent steady RANS approaches, fewer works explicitly integrate transition models such as the γ–Re_θ formulation to capture laminar-to-turbulent transition and separation behavior under low-Reynolds-number conditions.

Accordingly, the present study conducts a transition-model-based comparative aerodynamic analysis of four symmetric NACA airfoils (0012, 0015, 0018, and 0020) using a two-dimensional steady RANS framework coupled with the SST k–ω turbulence model and the γ–Re_θ transition model. By evaluating lift, drag, and aerodynamic efficiency across multiple Reynolds numbers and angles of attack, this work aims to provide improved comparative insight into transitional effects on airfoil performance and to support informed airfoil selection for small-scale wind energy and UAV applications.

Methodology

Governing Equations

The aerodynamic flow around the airfoils was modeled using a two-dimensional steady incompressible Reynolds-Averaged Navier–Stokes (RANS) framework. Since the operating conditions correspond to low-speed external aerodynamics, the flow was assumed incompressible with constant fluid properties.

Under these assumptions, the governing equations consist of the continuity and momentum equations expressed in tensor notation as follows:

$$\frac{\partial u_i}{\partial x_i} = 0 \quad \text{(Continuity equation)}$$

$$\rho u_j \frac{\partial u_i}{\partial x_j} = -\frac{\partial p}{\partial x_i} + \frac{\partial}{\partial x_j}\left[\mu\left(\frac{\partial u_i}{\partial x_j} + \frac{\partial u_j}{\partial x_i}\right)\right] + \frac{\partial}{\partial x_j}\left(-\overline{\rho u_i' u_j'}\right) \quad \text{(Momentum equation)}$$

where u_i represents the mean velocity components, p is the mean static pressure, ρ is the fluid density, μ is the molecular viscosity, and $-\overline{\rho u_i' u_j'}$ denotes the Reynolds stress tensor arising from turbulence modeling.

To close the RANS equations, the Reynolds stresses were modeled using the Boussinesq hypothesis, which relates the Reynolds stress tensor to the mean strain rate:

$$-\overline{\rho u_i' u_j'} = \mu_t\left(\frac{\partial u_i}{\partial x_j} + \frac{\partial u_j}{\partial x_i}\right) - \frac{2}{3}\rho k \delta_{ij}$$

where μ_t is the turbulent eddy viscosity, k is the turbulent kinetic energy, and δ_{ij} is the Kronecker delta.

Turbulence and Transition Modeling

The Reynolds stresses in the RANS equations were modeled using the Shear Stress Transport (SST) k–ω turbulence model. The turbulent eddy viscosity is computed as:

$$\mu_t = \frac{\rho k}{\omega} F_2$$

where k is the turbulent kinetic energy, ω is the specific dissipation rate, and F_2 is a blending function that limits turbulent viscosity in adverse pressure gradient regions.

The steady incompressible transport equations for k and ω are given by:

$$\rho u_j \frac{\partial k}{\partial x_j} = P_k - \beta^* \rho k \omega + \frac{\partial}{\partial x_j}\left[\left(\mu + \sigma_k \mu_t\right)\frac{\partial k}{\partial x_j}\right]$$

$$\rho u_j \frac{\partial \omega}{\partial x_j} = \alpha \frac{\omega}{k} P_k - \beta \rho \omega^2 + \frac{\partial}{\partial x_j}\left[(\mu + \sigma_k \mu_t) \frac{\partial \omega}{\partial x_j} \right] + 2(1 - F_1) \frac{\rho \sigma_{\omega 2}}{\omega} \frac{\partial k}{\partial x_j} \frac{\partial \omega}{\partial x_j}$$

where P_k represents turbulence production, and F_1 is the blending function that transitions between the k–ω and k–ε formulations.

Although the SST model performs well in separated flows, conventional turbulence models often fail to accurately capture laminar-to-turbulent transition at low Reynolds numbers, especially in the presence of laminar separation bubbles. To improve transition prediction, the SST model was coupled with the γ–Re_θ transition model.

The γ–Re_θ framework introduces two additional transport equations:

$$\rho u_j \frac{\partial \gamma}{\partial x_j} = P_\gamma - E_\gamma + \frac{\partial}{\partial x_j}\left[\left(\mu + \frac{\mu_t}{\sigma_\gamma} \right) \frac{\partial \gamma}{\partial x_j} \right]$$

$$\rho u_j \frac{\partial \mathrm{Re}_\theta}{\partial x_j} = P_\theta + \frac{\partial}{\partial x_j}\left[\sigma_\theta (\mu + \mu_t) \frac{\partial \mathrm{Re}_\theta}{\partial x_j} \right]$$

where γ controls turbulence intermittency and Re_θ determines transition, onset based on empirical correlations and local flow parameters.

The coupled SST–γ–Re_θ formulation enables distinction between laminar, transitional, and fully turbulent regions within the boundary layer, thereby enhancing predictive accuracy for low-Reynolds-number airfoil simulations compared to conventional fully turbulent RANS approaches.

Aerodynamic Coefficients

The lift force L and drag force D were obtained by integrating pressure and viscous stresses over the airfoil surface. The non-dimensional aerodynamic coefficients were computed as:

$$C_L = \frac{L}{0.5 * \rho * U_\infty^2 * S_{ref}}$$

$$C_D = \frac{D}{0.5 * \rho * U_\infty^2 * S_{ref}}$$

$$\text{Lift to Drag ratio} = \frac{C_L}{C_D}$$

Where S_{ref} is the reference area and U_∞ is the velocity of flow in the freestream.

Computational Domain

Geometry Specification

The computational procedure began with the generation of a two-dimensional flow domain around each symmetric NACA airfoil. A C-type topology was adopted to ensure smooth grid distribution and accurate resolution of the near-wall flow region. As illustrated in Figure 1, the outer boundaries of the computational domain were positioned at a distance of 15 chord lengths from the airfoil in all directions. This extended domain minimizes blockage effects and reduces artificial boundary interference on the aerodynamic solution.

Figure 2 presents the geometric configuration of the airfoils considered in this study. The maximum thickness of each NACA profile corresponds to its respective designation: 12% of the chord length for NACA 0012, 15% for NACA 0015, 18% for NACA 0018, and 20% for NACA 0020. A chord length of 1 m was used for normalization purposes in all simulations. The airfoil geometry was subtracted from the surrounding fluid domain using a Boolean operation to define the computational flow region.

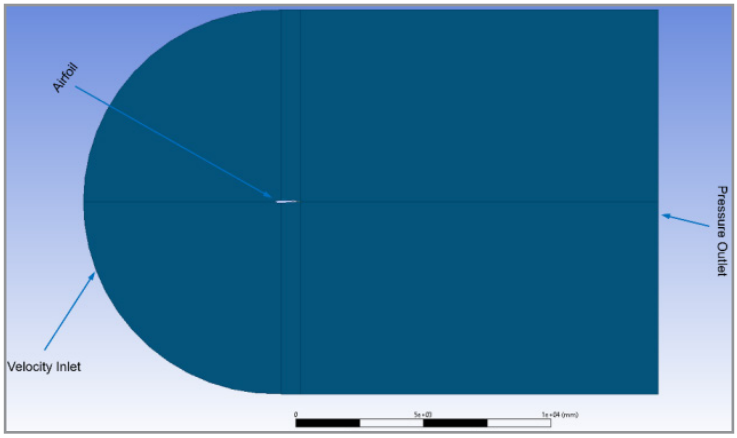

Figure 1: Computational domain and boundary extents around the airfoil.

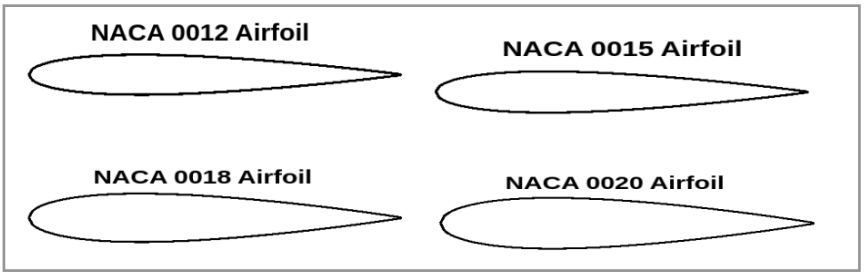

Figure 2: Geometric configuration of symmetric NACA airfoils (0012, 0015, 0018, and 0020).

To enhance solution accuracy, local grid refinement was applied around the airfoil surface through strategically placed projection lines. This approach ensured increased mesh density in regions where strong velocity gradients, pressure variations, and boundary-layer development occur.

Mesh Generation and Grid Independence

The meshing strategy plays a critical role in ensuring the accuracy and reliability of Computational Fluid Dynamics (CFD) simulations. A high-quality mesh must completely discretize the computational domain without gaps, overlaps, or distorted elements. Mesh topology, element size, and grid distribution directly influence numerical stability, convergence behavior, and solution accuracy, particularly when aerodynamic results are compared with experimental data.

Among available meshing approaches, structured, unstructured, and hybrid—structured meshing is generally preferred for external aerodynamic simulations due to its reduced numerical diffusion and improved solver efficiency. Structured grids typically employ quadrilateral elements in two-dimensional domains and hexahedral elements in three-dimensional configurations, which enhance numerical accuracy compared to triangular elements. In the present study, a structured quadrilateral mesh was adopted to achieve high solution accuracy with a comparatively lower cell count, consistent with findings reported in earlier investigations [16, 17].

Figures. 3 and 4 present the computational grid used in this study. Figure 3 illustrates the overall grid distribution across the computational domain, while Figure 4 provides a detailed view of the refined mesh near the airfoil surface. Grid clustering was applied in the vicinity of the airfoil to accurately resolve velocity gradients and boundary-layer development.

To properly capture near-wall behavior and potential laminar separation bubbles, the first cell height was selected to maintain a dimensionless wall distance of $y^+<1$. This near-wall resolution is essential for the accurate implementation of the SST k–ω turbulence model coupled with the γ–Re_θ transition model. The transition-sensitive modeling framework enables improved prediction of laminar-to-turbulent transition compared to conventional fully turbulent RANS approaches, while maintaining a reasonable computational cost relative to higher-fidelity methods such as LES and DES.

A mesh independence study was conducted to ensure that the numerical results were not sensitive to grid resolution. The mesh was progressively refined by increasing the number of grid elements until variations in the lift coefficient became negligible [18, 30]. As shown in Figure 5, approximately 200, 000 grid elements were sufficient to achieve grid-independent results at an angle of attack of 3° for NACA 0012. Further refinement produced insignificant changes in the aerodynamic coefficients, confirming the adequacy of the selected mesh density while maintaining computational efficiency.

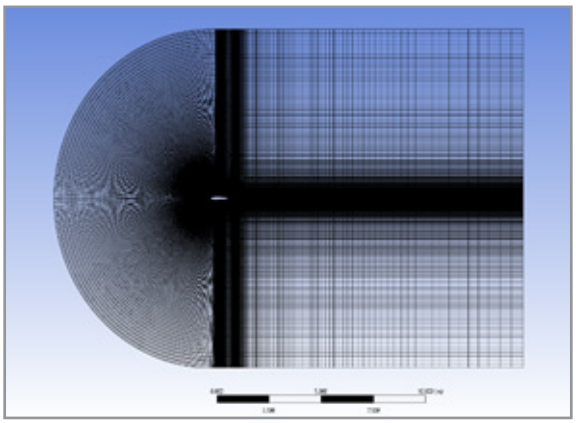

Figure 3: Structured quadrilateral mesh distribution over the entire computational domain.

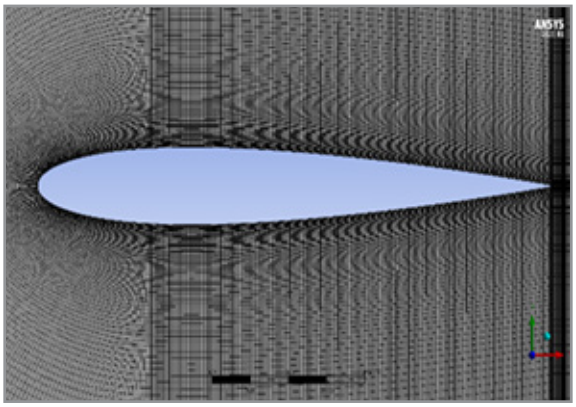

Figure 4: Close-up view of the grid distribution near the airfoil surface.

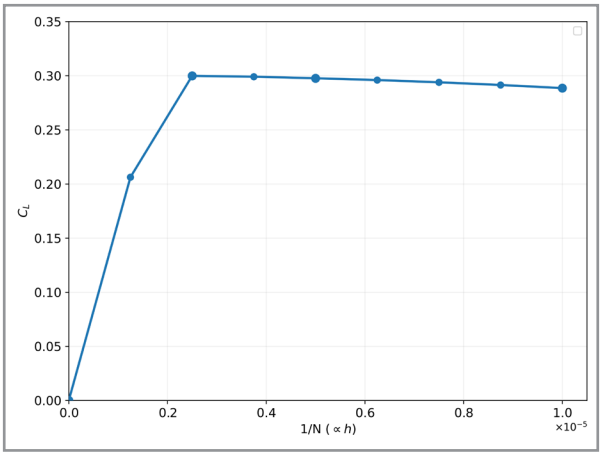

Figure 5: Mesh independence test.

Solver and Numerical Setup

The numerical simulations were performed using ANSYS Fluent to investigate the aerodynamic behavior of the selected symmetric NACA airfoils under low Reynolds number conditions. A two-dimensional, steady, pressure-based solver was employed in accordance with the incompressible flow assumption. ANSYS Fluent solves the integral form of the governing mass and momentum conservation equations [31].

Pressure–velocity coupling was handled using the coupled algorithm to enhance numerical stability and convergence efficiency [32]. Second-order upwind discretization schemes were applied to the momentum and turbulence transport equations to improve spatial accuracy. Gradients were evaluated using the least-squares cell-based method. Convergence was achieved when the residuals of all governing equations decreased below 10^{-6}, and the lift and drag coefficients exhibited negligible variation with additional iterations.

.

Although it is challenging to ensure that the simulation's operating conditions perfectly match those of wind tunnel experiments, the assumptions made in this study are validated by the strong agreement between the numerical and experimental results. The boundary conditions and key simulation parameters are summarized in Table 1.

Table 1: The boundary conditions are listed in the table below.

Boundary Conditions	Type
Fluid	Air
Flow Condition	Steady-state
Inlet	Velocity inlet
Outlet	Pressure outlet
Airfoil	Wall
Operating pressure	101325 Pa
Density of fluid	1.225 kg/m^3
Chord	1m
Reynolds Number	3× 10^5, 5× 10^5, 7× 10^5, 1× 10^6
Model	SST k-ω with γ–Re_θ transition
Viscosity	1.7894 × 10^{-5}
Angle of Attack	0°, 3°, 6°, 9°, 12°, 15°, 18°
Convergence factor	10^{-6}
Solver	Pressure Based

Results & Discussions

Validation

The numerical predictions for the NACA 0018 airfoil were validated against the experimental data reported by Timmer [11] at a Reynolds number of 1, 000, 000. The comparison of lift coefficient (C_L) and drag coefficient (C_D) variations with angle of attack (AOA) is presented in Figure 6. The numerical results closely follow the experimental trends across the investigated range of angles of attack. In the linear and pre-stall region (AOA ≤ 15°), the predicted lift curve slope and drag characteristics show strong agreement with the experimental measurements, indicating that the coupled SST k–ω and γ–Re_θ transition framework effectively captures boundary-layer development and transition behavior. The model successfully predicts the progressive increase in lift up to the stall angle, which occurs between 15° and 16°, consistent with the experimental observations. Slight divergence is observed beyond the stall region, particularly in drag prediction, which is expected due to the highly separated

and unsteady flow structures that are inherently challenging to resolve using steady RANS-based simulations. Overall, the close correspondence between numerical and experimental data confirms the reliability of the adopted turbulence–transition modeling approach. The validation results establish confidence in the numerical methodology and support its application in the subsequent comparative analysis of the selected airfoils.

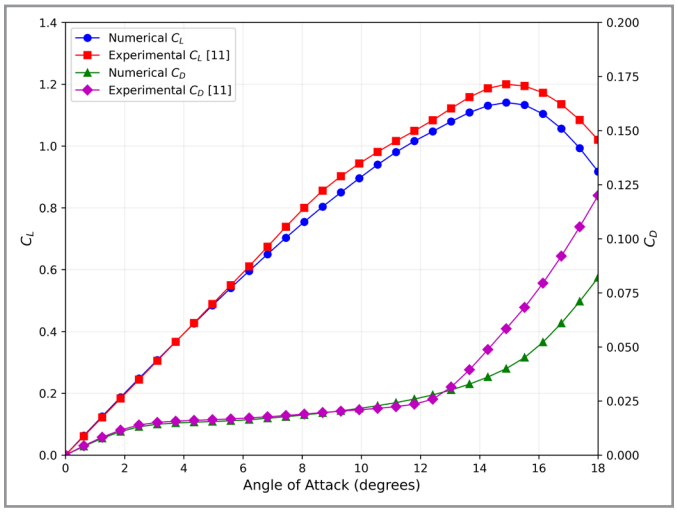

Figure 6: Validation of Numerical "C_L & C_D" with Experimental Data [11]

Results

Figures 7 to 14 present the variations of lift (C_L) and drag (C_D) with angle of attack for the four symmetric NACA airfoils across the investigated Reynolds number range. Overall, C_L increases with angle of attack up to the pre-stall region, while C_D remains relatively low at small angles and rises more rapidly at higher angles due to increased viscous losses and the onset of separation. In all cases, increasing Reynolds number generally improves aerodynamic performance by delaying separation and reducing relative viscous effects, leading to higher C_L and comparatively lower C_D in the pre-stall regime.

The reduction in aerodynamic efficiency with increasing airfoil thickness can be attributed to enhanced pressure drag and earlier boundary-layer separation. Thicker profiles generate stronger adverse pressure gradients on the suction surface, which promote earlier flow separation at low Reynolds numbers. Consequently, the drag component increases more rapidly for thicker airfoils as the angle of attack rises. Conversely, thinner airfoils such as NACA 0012 exhibit reduced form drag and improved boundary-layer stability, resulting in delayed separation and higher lift-to-drag ratios within the pre-stall region.

Among the airfoils, NACA 0012 consistently produces the most favorable aerodynamic behavior. As shown in Figures 7 to 14, it achieves comparatively high lift while maintaining the lowest drag across most angles of attack, which directly translates into superior aerodynamic efficiency. NACA 0015 also shows a clear increase in lift with Reynolds number and reaches its peak performance at moderate angles of attack; however, its drag penalty is higher than NACA 0012, resulting in a noticeable lift–drag tradeoff. NACA 0018 demonstrates strong lift generation, but with a higher drag coefficient than NACA 0012 and NACA 0015, indicating that the additional thickness increases aerodynamic losses under these operating conditions. NACA 0020 exhibits the least favorable aerodynamic response, showing comparatively lower lift and higher drag, which reduces its overall efficiency despite some improvement at higher Reynolds numbers.

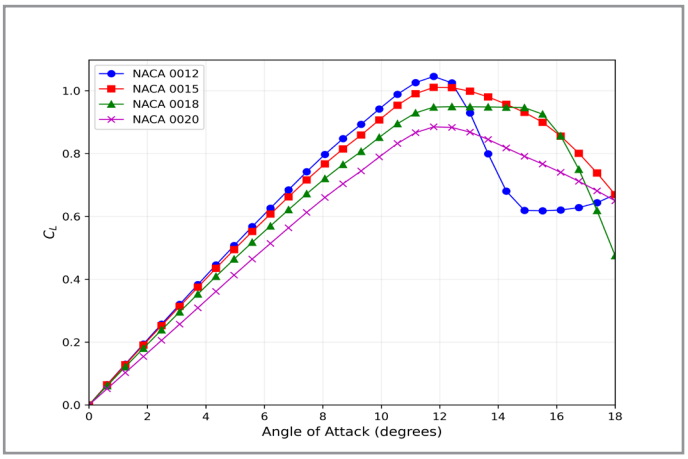

Figure 7: C_L Vs AOA for different NACA Profiles at Re= 300, 000

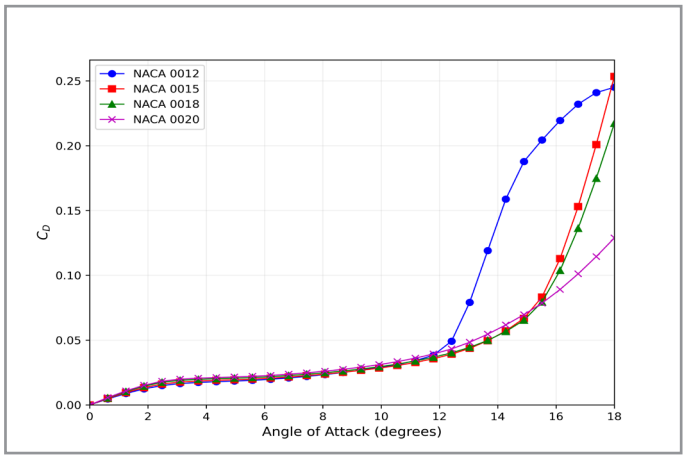

Figure 8: C_D Vs AOA for different NACA Profiles at Re= 300, 000

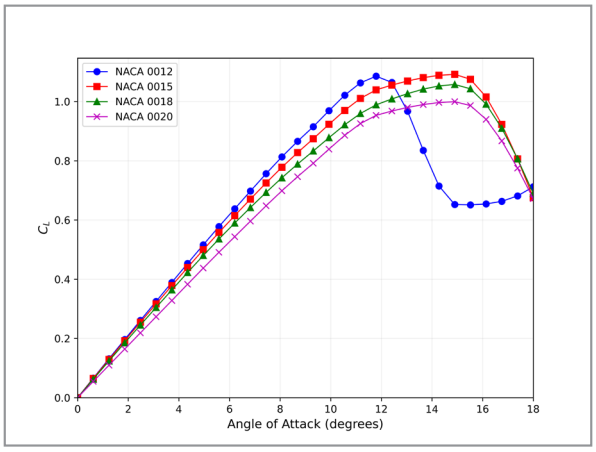

Figure 9: C_L Vs AOA for different NACA Profiles at Re= 500, 000

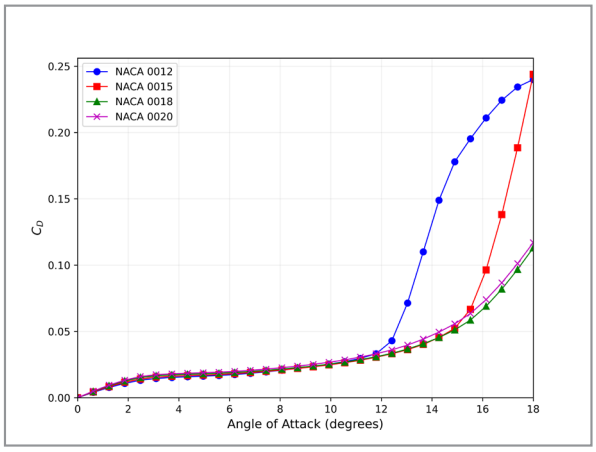

Figure 10: C_D Vs AOA for different NACA Profiles at Re= 500, 000

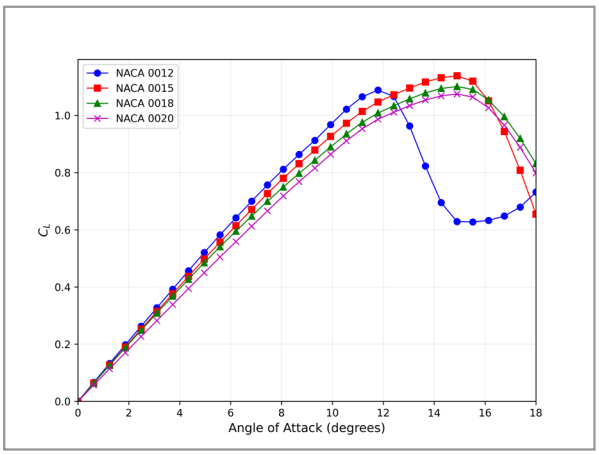

Figure 11: C_L Vs AOA for different NACA Profiles at Re= 700, 000

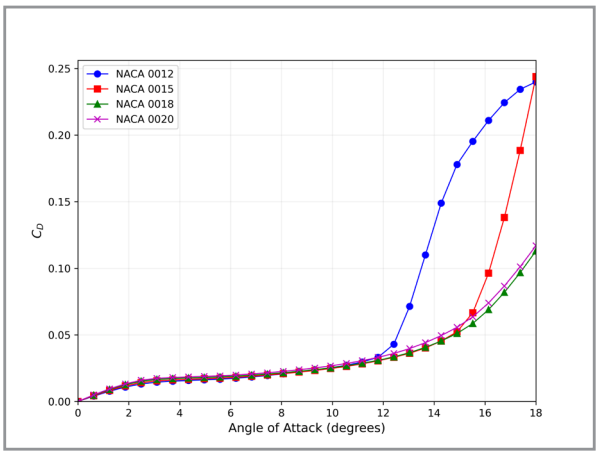

Figure 12: C_D Vs AOA for different NACA Profiles at Re= 700, 000

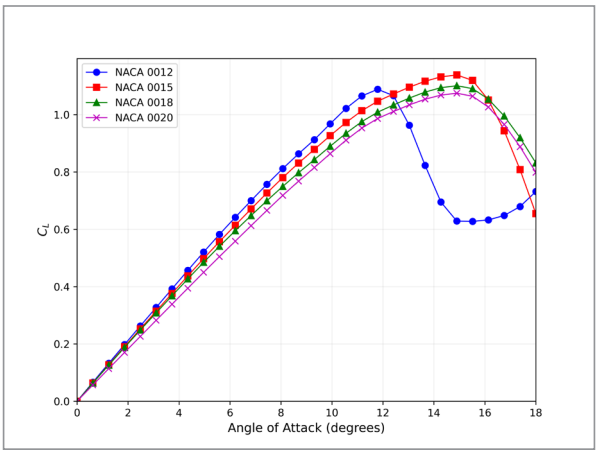

Figure 13: C_L Vs AOA for different NACA Profiles at Re= 1000, 000

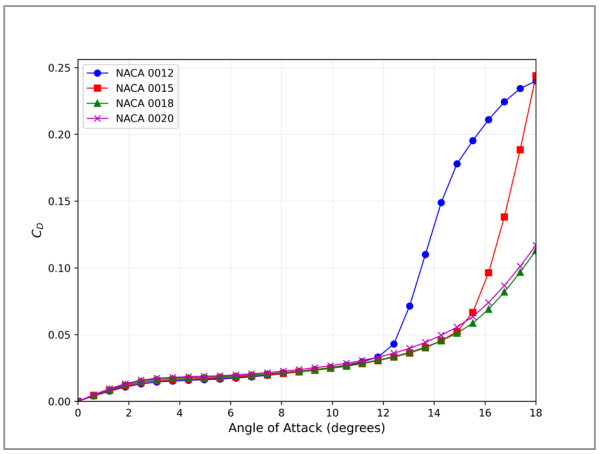

Figure 14: C_D Vs AOA for different NACA Profiles at Re= 1000, 000

Figures 15 to 18 provide airfoil-wise comparisons of aerodynamic efficiency using the lift-to-drag ratio (C_L/C_D). The results show that NACA 0012 achieves the highest C_L/C_D values across all Reynolds numbers, with peak efficiency consistently occurring in the moderate angle-of-attack range of approximately 6°–9°. NACA 0015 follows with relatively high C_L/C_D values but exhibits a sharper drop beyond its peak. NACA 0018 shows improved efficien-

cy with increasing Reynolds number, reflecting enhanced boundary-layer stability at higher Reynolds numbers, but its C_L/C_D remains below NACA 0012 due to the higher drag levels associated with increased thickness. NACA 0020 maintains the lowest C_L/C_D values across the range, and its efficiency decreases rapidly at high angles of attack, where drag growth becomes dominant.

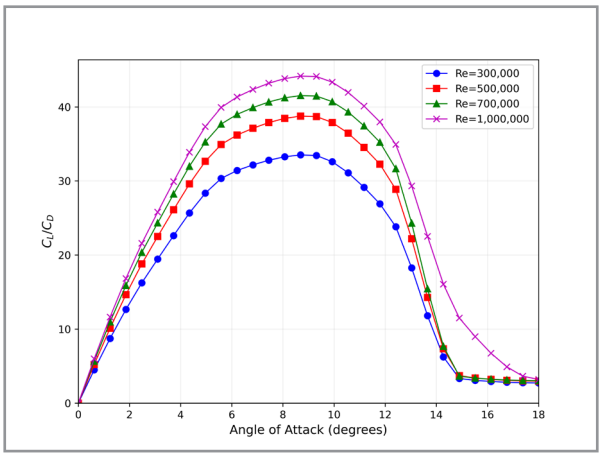

Figure 15: C_L/C_D Vs AOA for NACA 0012 Profiles at different Reynolds Numbers

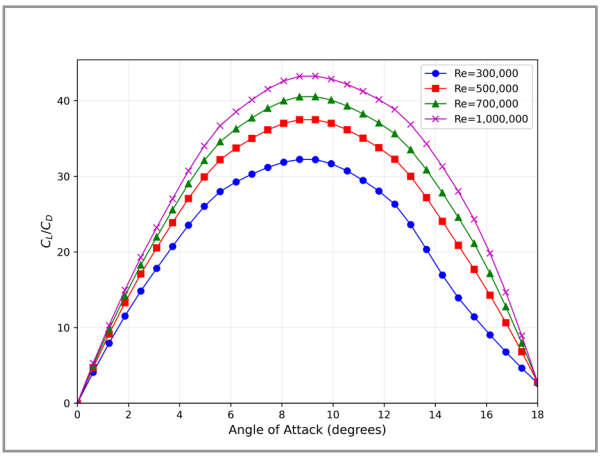

Figure 16: C_L/C_D Vs AOA for NACA 0015 Profiles at different Reynolds Numbers

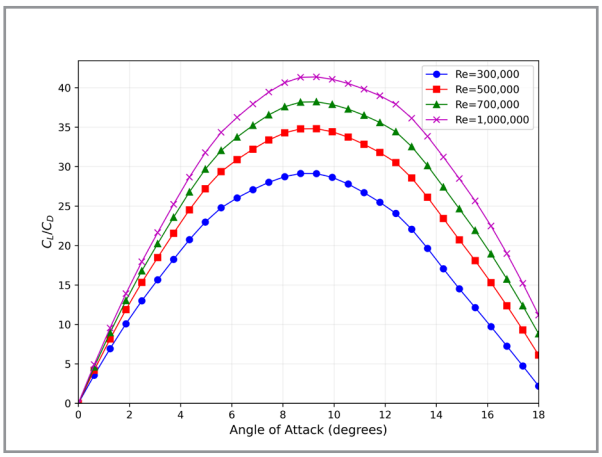

Figure 17: C_L/C_D Vs AOA for NACA 0018 Profiles at different Reynolds Numbers

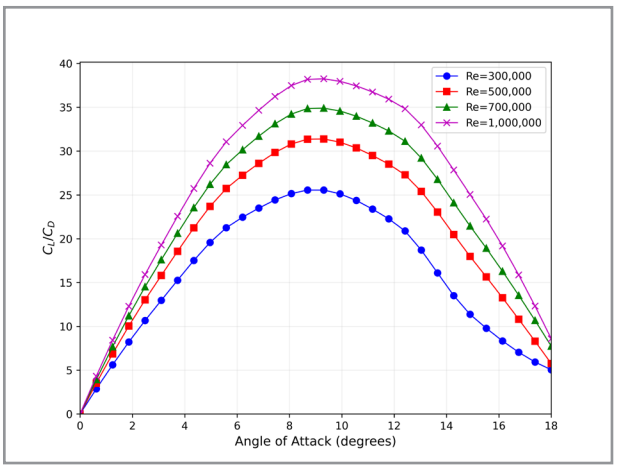

Figure 18: C_L/C_D Vs AOA for NACA 0020 Profiles at different Reynolds Numbers

Figures 19 to 22 compare C_L/C_D among the airfoils at each Reynolds number. Comparative analysis across Reynolds numbers confirms that peak aerodynamic efficiency consistently occurs at moderate angles of attack (6°–9°), beyond which separation-induced drag dominates. Across all Reynolds numbers, NACA 0012 remains the most efficient profile, whereas thicker airfoils show progressively lower C_L/C_D. These findings indicate that thinner symmetric airfoils are preferable when aerodynamic efficiency is the primary design objective, while thicker profiles may be considered where structural requirements or manufacturing constraints are prioritized, despite the associated efficiency penalty.

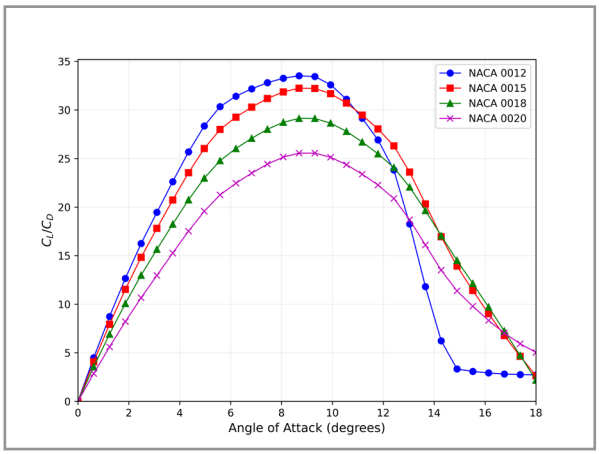

Figure 19: C_L/C_D Vs AOA for different NACA Profiles at Re= 300, 000

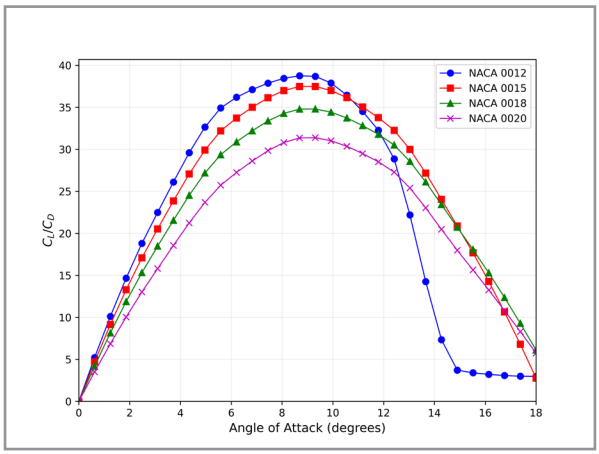

Figure 20: C_L/C_D Vs AOA for different NACA Profiles at Re= 500, 000

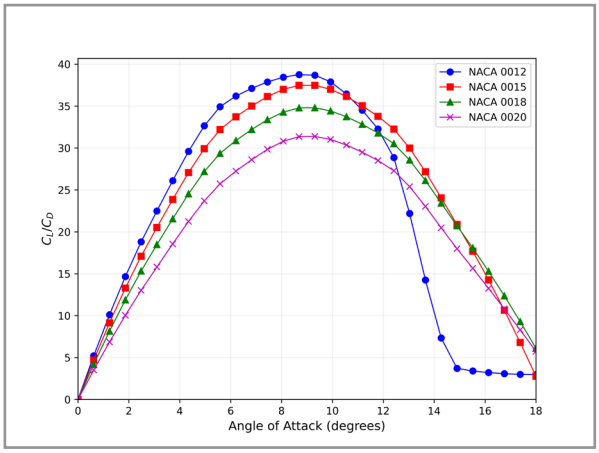

Figure 21: C_L/C_D Vs AOA for different NACA Profiles at Re= 700, 000

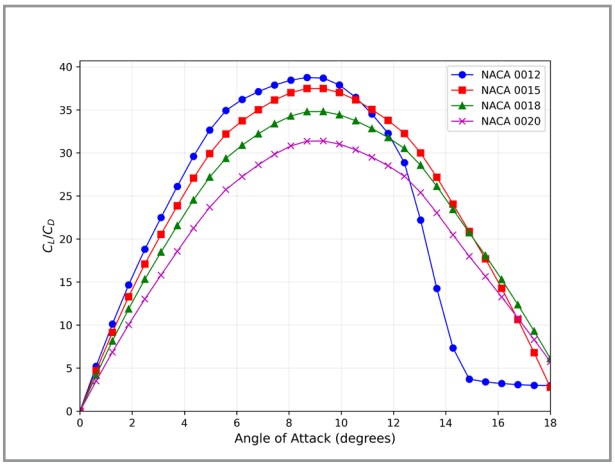

Figure 22: C_L/C_D Vs AOA for different NACA Profiles at Re= 1000, 000

Conclusions

This study presented a comparative computational investigation of the aerodynamic performance of symmetric NACA airfoils (0012, 0015, 0018, and 0020) under low Reynolds number conditions. A two-dimensional steady RANS framework was employed, incorporating the SST k–ω turbulence model coupled with the γ–Re_θ transition model to account for laminar-to-turbulent transition effects relevant to low-Reynolds-number aerodynamics. Validation against available experimental data demonstrated good agreement in the pre-stall regime, confirming the reliability of the adopted numerical approach for comparative analysis.

The results revealed a consistent improvement in aerodynamic performance with increasing Reynolds number, primarily due to delayed boundary-layer separation and reduced viscous influence. Among the investigated profiles, NACA 0012 exhibited the highest lift-to-drag ratios across all Reynolds numbers, with peak efficiency occurring at moderate angles of attack (approximately 6°–9°). NACA 0015 and NACA 0018 produced competitive lift characteristics but experienced higher drag penalties associated with increased thickness, resulting in comparatively lower aerodynamic efficiency. NACA 0020 demonstrated the lowest lift-to-drag performance due to its higher drag levels and earlier separation tendencies under the investigated operating conditions.

The findings highlight the sensitivity of low-Reynolds-number aerodynamic performance to airfoil thickness and boundary-layer transition behavior. Thinner symmetric profiles were found to be more suitable when aerodynamic efficiency is the primary design objective, whereas thicker profiles may be selected when structural considerations outweigh efficiency requirements.

While the present two-dimensional steady RANS framework provides reliable comparative insight in the pre-stall regime, post-stall predictions remain limited by steady-flow assumptions. Future investigations incorporating unsteady simulations and three-dimensional effects are rec-

ommended to further improve prediction fidelity for practical wind turbine and UAV applications.

Nomenclature	
Symbol	Definition
C_L	Lift coefficient
C_D	Drag coefficient
C_L/C_D	Lift-to-drag ratio
Re	Reynolds number
S_{ref}	Reference surface area
U_∞	Freestream velocity
ρ	Fluid density
p	Pressure
u	Velocity vector
AOA	Angle of Attack
RANS	Reynolds-Averaged Navier-Stokes
HAWT	Horizontal Axis Wind Turbine
VAWT	Vertical Axis Wind Turbine
CFD	Computational Fluid Dynamics

Acknowledgments
Not Applicable.

Authors' Contributions
The authors equally contributed to the conceptualization, methodology, simulation, data analysis, and manuscript preparation.

Funding
This research received no external funding.

Availability of Data and Materials
The raw data supporting the conclusions of this article will be made available by the authors on request.

Competing Interests
The authors have no conflicts of interest to disclose.

References

1. K. Kishinami, H. Taniguchi, J. Suzuki, H. Ibano, T. Kazunou, and M. Turuhami, "Theoretical and experimental study on the aerodynamic characteristics of a horizontal axis wind turbine," Energy, vol. 30, no. 11–12, pp. 2089–2100, 2005, doi: 10.1016/j.energy.2004.08.015.
2. P. Bhogle, A. Padalkar, S. Takke, M. Yedge, and S. Rasal, "Performance testing of NACA 0012 aerofoil by providing dimple surface," 2015, doi: 10.22214/ijraset.2017.4229.
3. W. W. Huebsch, P. D. Gall, S. D. Hamburg, and A. P. Rothmayer, "Dynamic roughness as a means of leading-edge separation flow control," J. Aircraft, vol. 49, no. 1, pp. 108–115, 2012, doi: 10.2514/1.C031350.
4. Dash, "CFD analysis of wind turbine airfoil at various angles of attack," IOSR J. Mech. Civ. Eng., vol. 13, no. 4, pp. 18–24, 2016, doi: 10.9790/1684-1304021824.
5. Shabur, A. Hasan, and M. Ali, "Comparison of aerodynamic behavior between NACA 0018 and NACA 0012 airfoils at low Reynolds number through CFD analysis," Adv. Mech. Eng. Technol., vol. 3, no. 2, pp. 1–8, 2020, doi: 10.5281/zenodo.4003677.
6. W. L. Siauw et al., "Transient dynamics of the flow around a NACA 0015 airfoil using fluidic vortex generators," Int. J. Heat Fluid Flow, vol. 31, no. 3, pp. 450–459, 2010, doi: 10.1016/j.ijheatfluidflow.2010.02.028.
7. G. R. Srinivasan, J. A. Ekaterinaris, and W. J. McCroskey, "Evaluation of turbulence models for unsteady flows of an oscillating airfoil," Comput. Fluids, vol. 24, no. 7, pp. 833–861, 1995, doi: 10.1016/0045-7930(95)00016-6.
8. M. Karthick and S. M. Kumar, "Investigation of aerodynamic performances of NACA 0015 wind turbine airfoil," Int. J. Eng. Res., vol. 5, no. 4, pp. 327–331, 2016, doi: 10.17950/ijer/v5s4/425.
9. M. Sereez et al., "Computational simulation of airfoils stall aerodynamics at low Reynolds numbers," in Proc. Royal Aeronautical Society Applied Aerodynamics Conf., Jul. 2016.
10. M. G. Lopes and J. A. V. Alé, "Numerical simulation of the aerodynamic characteristics of the NACA 0018 airfoil at medium range Reynolds number," Wind Eng., vol. 46, no. 6, pp. 1675–1688, 2022, doi: 10.1177/0309524X221102968.
11. W. A. Timmer, "Two-dimensional low-Reynolds number wind tunnel results for airfoil NACA 0018," Wind Eng., vol. 32, no. 6, pp. 525–537, 2008, doi: 10.1260/030952408787548848.
12. Dhiliban et al., "Aerodynamic performance of rear roughness aerofoils," in Proc. 8th Asia-Pacific Conf. Wind Eng., Chennai, India, Dec. 2013, doi: 10.3850/978-981-07-8012-8252.
13. S. K. Rasal and R. R. Katwate, "Numerical analysis of lift & drag performance of NACA0012 wind turbine aerofoil," Int. Res. J. Eng. Technol., vol. 4, no. 6, pp. 2892–2896, 2017.
14. M. N. K. Sahu, "Analysis of transonic flow over an airfoil NACA0012 using CFD," Int. J. Innov. Sci. Eng. Technol., vol. 2, no. 4, pp. 99–102, 2015.
15. D. C. Eleni, T. I. Athanasios, and M. P. Dionissios, "Evaluation of the turbulence models for the simulation of the flow over a NACA 0012 airfoil," J. Mech. Eng. Res., vol. 4, no. 3, pp. 100–111, 2012, doi: 10.5897/JMER11.074.

16. N. K. Lambropoulos, D. G. Koubogiannis, and K. C. Giannakoglou, "Acceleration of a Navier–Stokes equation solver for unstructured grids using agglomeration multigrid and parallel processing," Comput. Methods Appl. Mech. Eng., vol. 193, no. 9–11, pp. 781–803, 2004, doi: 10.1016/j.cma.2003.11.005.
17. D. R. Canonsburg, Fluent Theory Guide. ANSYS Academic Research, 2011.
18. H. Shah, S. Mathew, and C. M. Lim, "A novel low Reynolds number airfoil design for small horizontal axis wind turbines," Wind Eng., vol. 38, no. 4, pp. 377–391, 2014, doi: 10.1260/0309-524X.38.4.377.
19. D. C. Wilcox, Turbulence Modeling for CFD, vol. 2. La Canada, CA: DCW Industries, 1998.
20. F. R. Menter, M. Kuntz, and R. Langtry, "Ten years of industrial experience with the SST turbulence model," in Turbulence, Heat and Mass Transfer, vol. 4, no. 1, pp. 625–632, 2003.
21. J. McNaughton, F. Billard, and A. Revell, "Turbulence modelling of low Reynolds number flow effects around a vertical axis turbine at a range of tip-speed ratios," J. Fluids Struct., vol. 47, pp. 124–138, 2014, doi: 10.1016/j.jfluidstructs.2013.12.014.
22. Y. T. Lee and H. C. Lim, "Numerical study of the aerodynamic performance of a 500 W Darrieus-type vertical-axis wind turbine," Renew. Energy, vol. 83, pp. 407–415, 2015, doi: 10.1016/j.renene.2015.04.043.
23. J. Buchner et al., "Dynamic stall in vertical axis wind turbines: Comparing experiments and computations," J. Wind Eng. Ind. Aerodyn., vol. 146, pp. 163–171, 2015, doi: 10.1016/j.jweia.2015.09.001.
24. L. Daróczy et al., "Comparative analysis of turbulence models for the aerodynamic simulation of H-Darrieus rotors," Energy, vol. 90, pp. 680–690, 2015, doi: 10.1016/j.energy.2015.07.102.
25. P. Marsh et al., "Three-dimensional numerical simulations of straight-bladed vertical axis tidal turbines investigating power output, torque ripple and mounting forces," Renew. Energy, vol. 83, pp. 67–77, 2015, doi: 10.1016/j.renene.2015.04.014.
26. M. Jafaryar et al., "Numerical optimization of the asymmetric blades mounted on a vertical axis cross-flow wind turbine," Int. Commun. Heat Mass Transf., vol. 70, pp. 93–104, 2016, doi: 10.1016/j.icheatmasstransfer.2015.12.003.
27. R. Gosselin, G. Dumas, and M. Boudreau, "Parametric study of H-Darrieus vertical-axis turbines using CFD simulations," J. Renew. Sustain. Energy, vol. 8, no. 5, 2016, doi: 10.1063/1.4963240.
28. M. F. Ismail and K. Vijayaraghavan, "The effects of aerofoil profile modification on a vertical axis wind turbine performance," Energy, vol. 80, pp. 20–31, 2015, doi: 10.1016/j.energy.2014.11.034.
29. M. H. M. Mazumder, "Comparative study of turbulence models in CFD for transonic flow over the ONERA M6 wing," Discov. Mech. Eng., vol. 3, p. 46, 2024, doi: 10.1007/s44245-024-00080-5.
30. M. S. Genç, "Numerical simulation of flow over a thin aerofoil at a high Reynolds number using a transition model," Proc. Inst. Mech. Eng. C, vol. 224, no. 10, pp. 2155–2164, 2010, doi: 10.1243/09544062JMES2121.
31. ANSYS, Inc., ANSYS 14.5 User Guide, 2012.
32. F. J. Kelecy, "Coupling momentum and continuity increases CFD robustness," ANSYS Adv., vol. 2, no. 2, pp. 49–51, 2008.
33. F. R. Menter, "Review of the shear-stress transport turbulence model experience from an industrial perspective," Int. J. Comput. Fluid Dyn., vol. 23, no. 4, pp. 305–316, 2009, doi: 10.1080/10618560902773387.